Contents lists available at ScienceDirect

Journal of Volcanology and Geothermal Research

journal homepage: www.elsevier.com

Focal mechanisms of recent seismicity at Campi Flegrei, Italy

M. La Rocca [a,*], D. Galluzzo [b]

[a] Università della Calabria, Cosenza, Italy
[b] Istituto Nazionale di Geofisica e Vulcanologia – Osservatorio Vesuviano, Napoli, Italy

ARTICLE INFO

Article history:
Received 19 June 2019
Received in revised form 11 October 2019
Accepted 11 October 2019
Available online xxx

Keywords:
Focal mechanism
Campi Flegrei
Volcano-tectonic earthquake
Stress field
Ground uplift
High angle fault

ABSTRACT

The present study analysed volcano tectonic earthquakes that occurred in the caldera of Campi Flegrei, Italy from 2000 to 2019 to compute source focal mechanisms. We used data from a large number of seismic stations to estimate reliable fault plane solutions for 71 events of a maximum duration magnitude (M_D) ranging between $0.5 \leq M_D \leq 2.5$. We found that most solutions were of a normal type and were rake-angle negative focal mechanisms in 86% of the cases. Only a few earthquakes occurred on normal dip-slip faults; the majority occurred on varying degrees of oblique slip. Only one event had a pure reverse-mechanism, and it was located far from the caldera centre. The spatial distribution of the computed mechanisms exhibited a remarkable mix of fault orientations without any relationship to the location area or source depth. The predominance of normal kinematics on high-angle and nearly vertical faults and the very shallow source depth exhibited good agreement with the fact that seismicity at Campi Flegrei occurred during periods of ground uplift. In fact, ground uplift elongated the shallowest crust, thus reducing the normal stress on existing locked faults; this facilitated earthquakes, particularly those characterised by normal, dip-slip, and strike-slip mechanisms. In contrast, ground subsidence produced a horizontal shortening of the upper crust, which increased the normal stress on high-angle faults and reduced earthquake occurrence. Our results indicate that the driving force of the recent volcano-tectonic seismicity in the study region is the ongoing ground uplift.

© 2019.

1. Introduction

The investigation of fault geometry and kinematics in areas affected by small-to-medium sized earthquakes can improve our understanding of the mechanisms of local seismicity. This is notably important in volcanic environments, where the activation of pre-existing seismogenic sources may be the first consequence of renewed volcanic activity. Therefore, analysing small-to-medium size earthquakes in detail is a quite common practice in active volcano monitoring (e.g. Antayhua-Vera et al., 2015; Cardona et al., 2018; Judson et al., 2018; Hopp and Waite, 2016; Konstantinou et al., 2009; Li et al., 2019; Reyners, 2010; Roman et al., 2006). The aim of the present study is to evaluate and interpret the focal mechanisms and associated stress-fields of the volcano-tectonic (VT) earthquakes that occurred in the caldera of Campi Flegrei (hereafter CF), Italy, between 2000 and 2019.

The CF caldera is a complex volcanic field that has been active for ~80 ky (Vitale and Isaia, 2014). The main features of the current conditions at CF are the result of two major eruptions that were followed by caldera collapses: the Ignimbrite Campana and the Neapolitan Yellow Tuff (NYT), which occurred ~37 ky and ~12 ky ago, respectively (Orsi et al., 1999; Di Vito et al., 1999). After the NYT eruption, the activity was characterised by at least 70 eruptions, which pro-

* Corresponding author.
Email address: mario.larocca@unical.it (M. La Rocca)

https://doi.org/10.1016/j.jvolgeores.2019.106687
0377-0273/ © 2019.

UNCORRECTED PROOF

duced many craters that are easily recognisable inside the caldera. The last eruption in the area occurred in 1538 A.D. and resulted in the building of the Monte Nuovo crater (Di Vito et al., 2016). The structural setting of the CF caldera is delineated by the oldest calderas and crater rims along with an articulate network of fractures and faults (Vitale and Isaia, 2014). After the 1538 eruption, the CF caldera was characterised by a phase of slow ground subsidence that continued until 1950 (Del Gaudio et al., 2010). Alternating periods of slow ground uplift and subsidence, called bradyseism, constitute the most typical feature of the CF caldera. In recent years, two important episodes of bradyseism occurred during 1970–1972 and 1982–1984, and were characterised by ~3.5 m of maximum total ground uplift and intense seismicity. Slow ground subsidence started in 1985 and continued until 2000, and resulted in a total elevation decrease of > 1 m. In 2000 and 2006, a few minor episodes of ground uplift also occurred (a few cm), which were both accompanied by low magnitude seismicity (Saccorotti et al., 2001, 2007). Since 2006, slow uplift has occurred and is still ongoing at a rate of a few cm/year, thus leading to the declaration of a state of unrest in 2012. For this reason, and in consideration of the local high population density, the CF caldera is one of the highest risk volcanic areas in the world (Orsi et al., 2004, 2009).

In the past, uplift phases were accompanied by intense seismic activity, while subsidence phases were usually aseismic. The most important seismic event of the last century, which was characterised by more than 16 000 earthquakes with a maximum magnitude (M_D) of 4.2 (Aster et al., 1992), occurred during ground uplift between 1982 and 1984. The strongest and most well recorded of these earthquakes have been studied by several authors. Gaudiosi and Iannaccone (1984) estimated the focal mechanisms for 15 earthquakes and found a predominance of extensional dynamics. Whereas De Natale et al. (1995) and Orsi et al. (1999) found the prevalence of normal mechanisms with a small number of reverse sources. Similar results were reported by Saccorotti et al. (2007) for the earthquake swarm that occurred in 2006. The results of these analyses exhibited a wide distribution of fault orientations, with the most common strike-oriented being in the NW-SE and NE-SW directions. However, N–S and E–W directions are also populated. Structural studies of surface fractures and faults have confirmed the importance of such directions, and have provided estimations of the fault sizes ranging from tens of meters to a few hundred meters (Vitale and Isaia, 2014; Acocella, 2010).

Different hypotheses about the mechanisms of earthquake occurrence have been developed, and are mostly linked to ground uplift phenomenon. The presence of both normal and reverse faults is considered compatible with a shearing mechanism of resurgence (Orsi et al., 1999). Acocella (2010) hypothesised two different dynamics: a) bradyseism, which is characterised by moderate uplift and is accompanied by seismicity and hydrothermal manifestations, and b) caldera resurgence, which is identified by higher uplift, surface faulting, and eruptions. In this context, the occurrence of earthquakes in the central part of the caldera is associated with the shallow crust bending due to resurgence. D'Auria et al. (2011) suggest the role of fluids in driving the occurrence of VT earthquakes through an increase of fluid pore-pressure and a decrease in normal stress.

In the present study, increased performance of seismic monitoring, both in terms of available seismic stations and data quality (La Rocca and Galluzzo, 2012, 2015) , allowed us to estimate the focal mechanism of VT earthquakes as small as $M_D = 0.5$. Here, we present the results obtained for 71 VT earthquakes in the CF caldera, which occurred between 2000 and 2019 and have magnitude in the range $0.5 \leq M_D \leq 2.5$.

2. Recent seismicity

The epicentres and depth distribution of VT earthquakes with $M_D > 0$ that occurred from 2000 to 2019 are shown in Fig. 1. Fig. 1b shows the depth distributions of VT earthquakes selected for $M_D \geq 0$ (707 events), $M_D \geq 1$ (100 events), and $M_D \geq 2$ (8 events). Ninety percent of all events were located at shallow depths between 0.5 km and 2.5 km below sea level. Two events were deeper than 4 km and no events were deeper than 5 km. The ongoing ground uplift in the CF caldera has been characterised by a roughly circular pattern centred at the town of Pozzuoli, as shown, for example, by De Martino et al. (2014a, their Fig. 6) and by Iannaccone et al (2018). Most seismic events have been located in the central part of the caldera, where ground uplift shows the highest values. Fig. 2 shows the temporal evolution of ground uplift and VT seismicity. The ground level variation at the reference global positioning system (GPS) station in Pozzuoli (shown in Fig. 1, and also see De Martino et al., 2014a, 2014b) is shown in Fig. 2a. The weekly numbers of VT earthquakes from 2000 to 2019 are shown in Fig. 2b, and the magnitudes are shown in Fig. 2c. A tight correlation between seismicity and ground uplift is evident in Fig. 2, which has also been noted by other studies (Orsi et al., 1999; D'Auria et al., 2011). From 2006 to 2019, the central part of the CF caldera raised by > 50 cm. During the last 15 years, the seismicity rate has increased, and roughly followed the uplift trend and included several swarms of VT events. The increased seismicity during the last decade in comparison to previous

UNCORRECTED PROOF

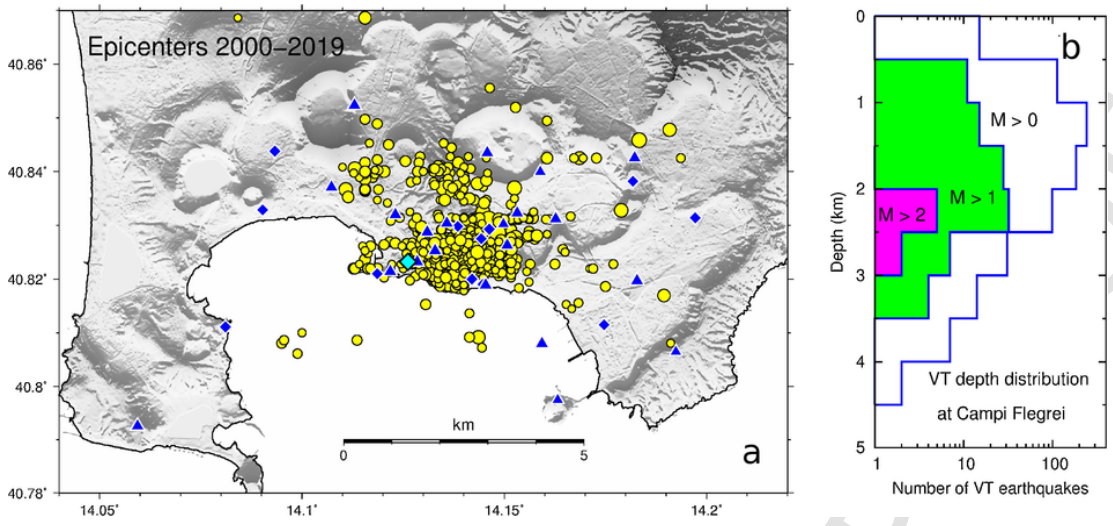

Fig. 1. a) Map of the Campi Flegrei area showing seismic stations (blue symbol), reference RITE global positioning system (GPS) station (cyan symbol), and epicentres of volcano-tectonic (VT) earthquakes with a maximum magnitude $M_D > 0$ from 2000 to 2019 (707 events shown by yellow symbol, whereby the size is proportional to the magnitude). b) Depth distribution of VT earthquakes. (For interpretation of the references to colour in this figure legend, the reader is referred to the web version of this article).

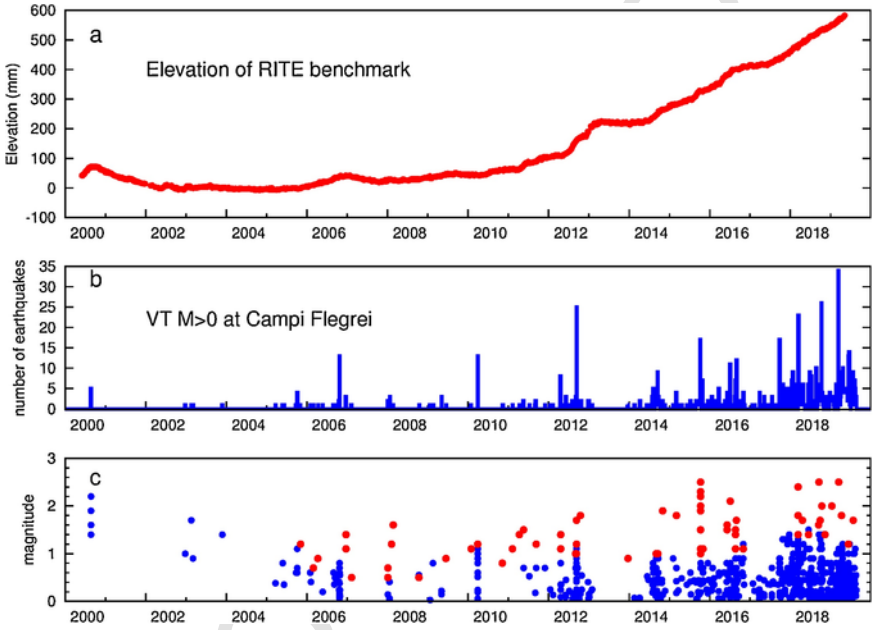

Fig. 2. a) Ground level elevation from 2000 to 2019 at the reference global positioning system (GPS) station RITE in Pozzuoli town (see Fig. 1 for the position of the RITE station), b) weekly number of volcano-tectonic (VT) earthquakes, and c) magnitudes of the VT earthquakes. Red symbol shows the events for which the focal mechanism was computed. (For interpretation of the references to colour in this figure legend, the reader is referred to the web version of this article).

years is clearly visible in Fig. 2. Only for extremely small events (i.e. $M_D < 0$) is the increased rate likely to be due to the increased detection capability of the local seismic network (La Rocca and Galluzzo, 2015). However, such small earthquakes are not considered in the present study. From Fig. 2c we argue that the catalogue is complete down to $M_D = 0$ since at least 2012, probably earlier. Events during the last decade were located with fairly high precision and had i) an average root mean square (rms) value of between 0.04–0.12 s, ii) a horizontal location error in the range 0.2–0.3 km, and iii) an average vertical location error of < 0.5 km (Table 1). The magnitude of recent seismicity at CF is rarely > 2, but the shallow location means that such events can be felt as ground shaking with an audible rumble near the epicentre. Events shown

Table 1
Results of focal mechanisms analysis.

Origin time	lat	lon	Dep (km)	M_D	DH (km)	DZ (km)	rms (s)	gap	P/SV/SH	strike	dip	rake
20190611041755	40.82701	14.1353	2.67	1.2	0.34	0.68	0.139	47	13/8/7	270	57	−20
20190410225647	40.8309	14.1438	1.65	1.8	0.18	0.22	0.041	72	16/9/12	45	69	−47
20190315042641	40.8322	14.1484	2.36	2.5	0.21	0.27	0.067	55	25/4/4	231	64	−56
20181112212032	40.8332	14.1451	1.94	1.4	0.28	0.26	0.097	108	20/9/6	225	66	−65
20180928065947	40.8307	14.1274	3.24	1.7	0.31	0.36	0.090	112	13/6/8	280	15	−70
20180918213641	40.828	14.1473	2.29	2.5	0.34	0.26	0.112	43	22/8/11	60	88	47
20180915092356	40.8106	14.1403	3.00	1.6	0.43	0.32	0.072	103	12/4/4	275	50	−87
20180614215737	40.8268	14.1397	1.02	1.4	0.16	0.31	0.043	55	12/4/4	95	84	88
20180421042617	40.8309	14.1407	1.43	1.7	0.26	0.28	0.042	101	20/1/2	300	38	−35
20180312140906	40.8305	14.1498	2.99	2.4	0.30	0.29	0.057	50	20/4/7	268	46	−88
20180312135805	40.8366	14.1462	2.00	1.8	0.31	0.31	0.097	78	15/4/8	235	54	−61
20180312135013	40.8303	14.1494	2.15	1.4	0.13	0.14	0.035	61	18/2/3	263	63	−59
20180312134123	40.8292	14.1497	2.06	1.4	0.12	0.13	0.021	76	15/1/2	266	63	−62
20161030065653	40.8265	14.1307	1.98	1.1	0.20	0.24	0.095	59	12/11/6	295	15	−80
20160829154540	40.8327	14.1496	2.05	1.7	0.25	0.19	0.081	58	25/6/12	238	63	−64
20160823022257	40.8268	14.1383	2.37	1.5	0.08	0.10	0.026	41	21/11/7	166	86	−17
20160823021637	40.8273	14.1377	2.47	1.1	0.20	0.32	0.088	40	21/4/9	107	81	−58
20160823021500	40.8267	14.1375	2.18	1.4	0.20	0.28	0.043	41	23/3/5	133	57	−50
20160823020046	40.8260	14.1382	1.87	1.5	0.17	0.20	0.039	42	23/2/8	114	47	−58
20160705012239	40.8267	14.1312	2.07	2.1	0.18	0.18	0.045	70	21/4/6	93	61	−73
20160604024558	40.8242	14.1274	1.80	1.6	0.18	0.27	0.088	109	19/8/9	342	80	−35
20160604023853	40.8234	14.1274	1.74	1.5	0.18	0.31	0.089	117	19/1/1	318	81	−40
20151029224903	40.8432	14.1335	1.12	1.1	0.12	0.15	0.050	138	13/3/8	309	60	17
20151007091624	40.8337	14.1481	1.93	1.1	0.18	0.23	0.071	62	14/3/3	282	62	−15
20151007091050	40.8317	14.1462	2.26	2.5	0.20	0.21	0.059	50	25/4/7	248	68	−48
20151007084908	40.8338	14.1489	1.94	1.1	0.19	0.21	0.073	128	10/3/5	180	44	−60
20151007081351	40.8316	14.1472	2.03	2.3	0.19	0.19	0.103	51	26/3/8	240	62	−51
20151007080251	40.8329	14.1480	1.97	1.0	0.21	0.21	0.082	108	14/1/6	273	50	−43
20151007075908	40.8328	14.1483	1.96	1.1	0.16	0.16	0.057	58	20/4/10	240	61	−60
20151007075413	40.8330	14.1473	2.06	2.0	0.18	0.17	0.111	57	27/7/13	240	60	−52
20151007073740	40.8323	14.1465	1.96	2.2	0.19	0.18	0.118	53	23/8/12	266	63	−32
20151007073132	40.8319	14.1474	1.92	1.9	0.13	0.12	0.047	53	19/7/11	240	62	−60
20151007072618	40.8326	14.1478	2.02	1.0	0.18	0.21	0.090	56	14/3/9	246	64	−54
20151007072454	40.8316	14.1502	1.94	1.1	0.14	0.12	0.041	53	11/1/7	318	62	−80
20151007072034	40.8316	14.1466	2.47	1.5	0.32	0.33	0.132	51	11/1/5	264	87	20
20150303224947	40.8327	14.1498	2.05	1.8	0.14	0.14	0.044	59	17/4/12	281	47	−52
20141030125446	40.8263	14.1416	1.89	1.9	0.20	0.22	0.040	54	16/7/7	4	80	−12
20140916014512	40.8249	14.1351	2.20	1.0	0.22	0.28	0.085	114	12/6/3	307	49	−20
20140916012119	40.8226	14.1347	2.16	1.0	0.26	0.40	0.112	139	12/8/6	298	86	−15
20140904185403	40.8284	14.1171	1.91	1.0	0.17	0.25	0.083	75	3/6/5	83	74	−40
20131222002835	40.8667	14.1130	2.96	0.9	0.32	0.56	0.091	195	12/1/2	358	47	−83
20121016000552	40.8265	14.1455	1.73	1.8	0.15	0.16	0.040	62	23/5/8	271	11	−63
20120907084700	40.8354	14.1157	3.00	1.0	0.31	0.21	0.079	106	12/1/6	257	75	−84
20120907082500	40.8351	14.1114	3.01	1.7	0.34	0.34	0.077	105	17/4/8	272	52	−65
20120907080327	40.8353	14.1185	3.07	1.2	0.39	0.57	0.121	134	10/5/7	330	70	−80
20120907073414	40.836	14.111	3.0	1.7	0.34	0.30	0.077	107	15/1/6	304	75	4
20120901043738	40.8313	14.1120	2.36	1.0	0.21	0.26	0.040	75	10/4/4	129	36	−34
20120901040231	40.8327	14.1126	2.14	1.0	0.44	0.42	0.095	81	11/4/6	230	62	−65
20120420044553	40.8264	14.1343	1.92	1.1	0.25	0.31	0.110	103	14/7/8	152	67	−10
20120420042929	40.8224	14.1309	2.30	1.1	0.27	0.34	0.094	106	13/7/4	310	40	−50
20120419195642	40.824	14.133	2.1	1.4	0.20	0.28	0.058	114	16/3/6	316	70	−5
20110908025611	40.823	14.146	1.9	1.2	0.23	0.25	0.067	94	12/3/6	58	65	−7
20110519003955	40.842	14.177	3.1	1.5	0.19	0.16	0.024	241	9/4/5	96	85	−83
20110410121011	40.879	14.111	4.4	1.4	0.28	0.33	0.054	236	10/4/2	320	42	68

UNCORRECTED PROOF

Table 1 (*Continued*)

Origin time	lat	lon	Dep (km)	M_D	DH (km)	DZ (km)	rms (s)	gap	P/SV/SH	strike	dip	rake
20110207070303	40.845	14.135	1.7	1.1	0.41	0.59	0.098	191	8/0/0	324	90	25
20101106162101	40.870	14.086	4.9	0.8	1.2	1.5	0.08	319	6/4/6	193	40	−20
20100330164023	40.835	14.152	3.1	1.2	0.36	0.51	0.104	103	11/2/5	250	35	−88
20100129173448	40.855	14.150	3.1	1.1	0.39	0.55	0.113	285	7/3/6	22	90	90
20090613034044	40.827	14.145	2.0	0.9	0.31	0.38	0.074	86	9/1/2	61	68	−24
20081010115659	40.842	14.140	1.9	0.5	0.22	0.30	0.030	178	5/2/3	220	84	30
20080219124841	40.849	14.182	3.9	1.6	0.20	0.28	0.067	287	6/0/1	275	50	−5
20080204204634	40.841	14.120	1.7	1.2	0.25	0.22	0.081	197	8/0/0	88	45	−43
20080105191756	40.827	14.147	2.3	0.7	0.31	0.29	0.084	81	7/2/3	35	75	−30
20080105191728	40.829	14.149	2.0	0.5	0.33	0.28	0.097	85	8/2/2	10	70	−25
20070208010741	40.828	14.137	1.9	0.5	0.34	0.30	0.112	78	5/1/2	107	63	−44
20061221224215	40.842	14.145	1.2	1.1	0.15	0.13	0.051	122	8/5/4	162	80	−75
20061221222531	40.843	14.146	1.6	1.4	0.21	0.22	0.074	120	10/4/3	346	66	−40
20061220235305	40.827	14.154	3.1	1.1	0.24	0.16	0.069	106	9/2/2	48	23	−35
20060408070932	40.829	14.147	2.3	0.9	0.28	0.31	0.058	84	11/1/3	248	81	−38
20060301145601	40.839	14.121	1.6	0.7	0.29	0.29	0.037	244	5/2/2	190	42	−30
20051105061618	40.832	14.146	3.1	1.2	0.22	0.27	0.044	88	8/0/1	185	85	−85

Results of the focal mechanism analysis of 71 earthquakes. The table contains: origin time, latitude, longitude, depth, magnitude, horizontal location error, depth location error, rms, gap, P/SV/SH polarities used for the computation of focal mechanism, strike, dip, rake.

UNCORRECTED PROOF

by red symbols in Fig. 2c are those for which we computed the focal mechanism.

3. Data analysis and results

Computation of focal mechanisms and/or moment tensors are part of the routine analysis of earthquake data. For medium to large events they are routinely estimated by comparing observed signals to synthetic signals. The estimation of focal mechanisms, however, becomes less reliable and more difficult as the magnitude decreases. This happens because small earthquakes are recorded only at short distances, thus adequate coverage of the focal sphere is rarely achieved by local or regional networks. Moreover, small earthquakes produce mostly high frequency signals that are difficult to fit to synthetic waveforms. For a volcanic environment that is typically characterised by highly heterogeneous structures, the generation of high-frequency synthetic signals is further complicated by the number of scattered signals and site effects, which are very difficult to account for. For these reasons, the estimation of moment tensors of VT earthquakes of $M_D < 3$ through the comparison of observed signals and synthetic seismograms is challenging. In such cases, the computation of the fault plane solution through methods based on the polarity of direct waves remains the most effective analysis technique.

The seismic monitoring network in the CF area has improved greatly over the last 15 years, increasing from 10 analogue stations in 2000 (Castellano et al., 2002) to about 30 stations in 2015 (La Rocca and Galluzzo, 2012, 2015) and during the present study, as shown in Fig. 1. These include a few stations that were not operating at the time of the present study, but for which data were used for the analysis of past earthquakes. This high number of stations means that earthquakes as small as $M_D = 0.5$, located in the central part of the caldera, may have been recorded by more than 15 stations that are situated around the epicentre and at distances of up to 6–8 km. Most of the VT events are located at depths of between 0.5–3 km below sea level (Fig. 1). Such a shallow location is advantageous for the computation of focal mechanisms because the focal sphere is better constrained by direct wave paths, and even the lower hemisphere of the focal sphere may be sampled by the farthest stations.

We selected more than 90 VT earthquakes with $0.5 \leq M_D \leq 2.5$ recorded between 2000 and 2019 to estimate their focal mechanisms using the FOCMEC software (Snoke et al., 1984; Snoke, 1989), which allows for the use of the polarity of P, SV, and SH waves. After source location, the second step of our analysis involved the rotation of horizontal components in the radial and transverse directions. Although the determination of polarity for P waves is straightforward, this is not generally the case for SV and SH waves. When the P-wave polarity is clear at a sufficient number of stations that are well distributed on the focal sphere, the focal mechanism may be well-constrained without the need to consider SV and SH waves. An example of such a case is shown in Fig. 3, where the beach-ball plot obtained from the P-wave polarity of 17 stations is shown together with seismograms and their corresponding positions on the focal sphere. On the contrary, for other earthquakes, the number of P-wave polarities and their position on the focal sphere are insufficient for constraining the focal mechanism solution. In such cases, the use of the polarities of SV and SH waves strongly increases the chances of obtaining a well-constrained solution.

In many instances, observations of integrated signals (ground displacement) and causal filtered waveforms were very helpful for our estimations of SV and SH wave polarities. An example of the seismograms used to read the polarities of SV and SH waves is shown in Fig. 4, whereby the three wave components of four stations are shown in their original forms, and after integration and causal bandpass filtering. The observation of ground displacement makes it much easier to recognise the polarity of SV waves, which are seen on the radial and often on the vertical components, and the polarity of SH waves, which are expected to appear on the transverse component. Positive (cyan) and negative (green) polar-

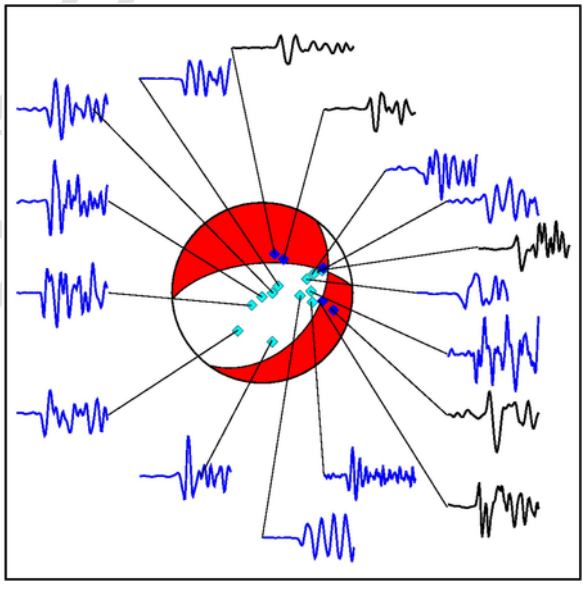

Fig. 3. P-wave of earthquake 20180312134123 as recorded at 17 seismic stations and the beach-ball plot that fit all polarities. Seismograms with negative first P-motion are shown in blue, while those with a positive onset are shown in black. (For interpretation of the references to colour in this figure legend, the reader is referred to the web version of this article).

UNCORRECTED PROOF

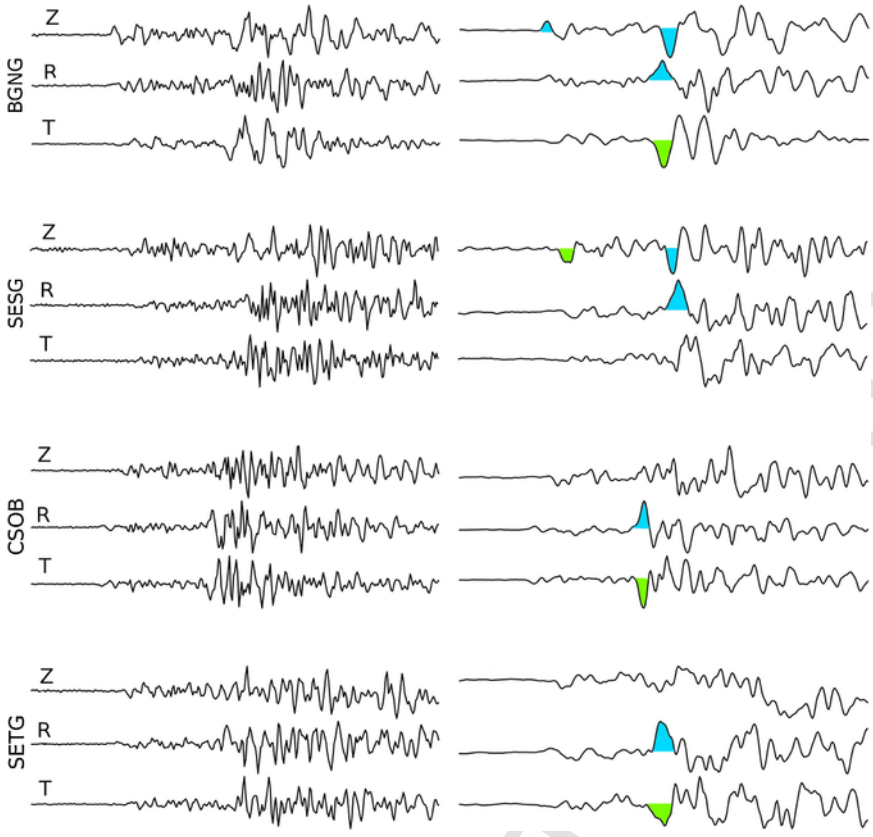

Fig. 4. Seismograms of earthquake 20160829154540 at four seismic stations. For each station the vertical, radial, and transverse components are shown in their original form in the left column, and after integration on the right side. A one-pole Butterworth causal bandpass filter (0.2–20 Hz) was applied to remove possible disturbances at very low and very high frequencies. Positive polarity is shown in cyan, while negative pulses are shown in green. (For interpretation of the references to colour in this figure legend, the reader is referred to the web version of this article).

ity pulses are shown in Fig. 4. In this example, the SV wave polarity was recognised at all four stations, whereas the SH wave polarity was considered as being clear in only three cases. We note that the SV wave, if seen on both radial and vertical components, must have opposite polarity on the two seismograms. There is a clear benefit of using the polarities of S waves in such cases because the number of observations increases, and thus provides more constraint on the focal mechanism solution. For example, in Fig. 4, the P wave is unrecognisable at stations CSOB and SETG. In fact, the pulse that is visible in the vertical signal (Z) starts after the first pulse in the radial component (R). This means that the direct P-wave at these two stations had a lower amplitude than the amplitude of the seismic noise in the vertical component, thus it cannot be used for phase picking or for polarity reading. In such cases, the polarity of SV and SH waves may be very important for achieving the final solution. Many of the selected events remained undetermined due to the insufficient coverage of the focal sphere with the available observed phase polarity.

We were able to compute reliable focal mechanisms for 71 VT earthquakes recorded from 2005 to 2019. Results are summarised in Table 1 and shown through a beach-ball plot in Fig. 5. For most of these earthquakes, the solution was well constrained, with uncertainty in the order of 10°-15° for the estimated strike, dip, and rake orientations. Only for a few events was the solution affected by uncertainty up to 30° on one or two of the three angles. This usually happens for i) events that were characterised by poor data quality, ii) events that has a lower magnitude, iii) events that were recorded by less than 10 stations, and/or iv) events that were located with large station gap. The increased number of stations after 2008 allowed for a better identification of the source location and for improved sampling of the focal sphere, thereby increasing the reliability of the estimations of the focal mechanisms. Earthquakes that occurred after 2010 in the central area of the caldera were located with gaps usually < 90°, and the estimation of focal mechanisms thus becomes more feasible and reliable for most of events with M_D >

UNCORRECTED PROOF

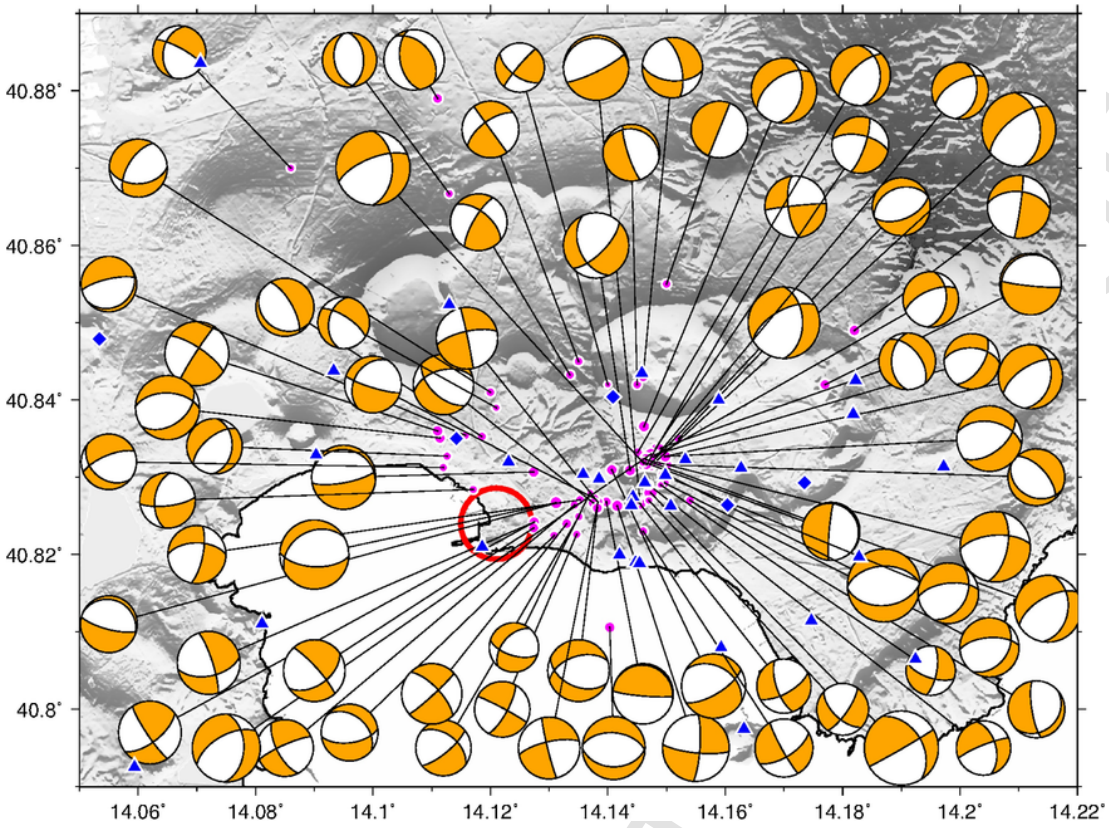

Fig. 5. Results of the focal mechanism analysis. Blue symbols represent the seismic stations used in this analysis and/or those that are currently installed. The size of beach-ball plots is proportional to the magnitude ($0.5 \leq M_D \leq 2.5$). The red circle shows the centre of Pozzuoli town. See also Table 1. (For interpretation of the references to colour in this figure legend, the reader is referred to the web version of this article).

1.2. In a few particularly favourable cases, we were even able to find good solutions for events as small as $M_D = 0.5$. On the contrary, computing a reliable solution for small earthquakes located in the gulf of Pozzuoli remains challenging due to the large location gap.

Given the ambiguity between the fault plane and auxiliary plane solutions, we considered both in order to perform a statistical analysis of the results. Therefore, hereafter we deal with 142 solutions that are representative of 71 earthquakes. Dip, rake, and strike angles versus time are shown in Fig. 6a, c and e, respectively, and their histogram distributions are shown in Fig. 6b, d, and f, respectively. The distributions of dip and rake values are strongly asymmetric (Fig. 6b, d); 75% of the plane solutions had a dip > 45°, 24% had a dip > 75°, whereas 86% had a rake < 0°. Hence, the most predominant focal mechanism was of a normal type, and most of the fault planes had a high dip-angle. However, there were a few pure normal-faults because most of the solutions with a rake angle < 0° had a significant oblique component (-180° < rake < -120°, and -60° < rake < 0°). Moreover, several solutions could be classified as dip-slip and strike-slip events (Figs. 5 and 7). On the contrary, no solutions with a pure reverse-mechanism were observed in the central part of the caldera. Only one such event was observed and it was located several km north (Fig. 5). The strike distribution (Fig. 6f) is much more uniform in comparison to the dip and rake distributions, but it still shows variability with some maxima (0°–30° and 240°–270°) and some minima (120°–150° and 180°–210°). The features of the computed focal mechanisms were synthesised in the ternary graph representation (Frohlich, 1992) shown in Fig. 7. The predominance of normal kinematics is clearly evident in this plot, where most of the solutions are amassed along the right side of the graph.

Since most of the analysed earthquakes were located in the central part of the caldera, where seismicity, ground deformation, and gas emissions are reportedly higher (Cardellini et al., 2017), we focused on looking for common features and a possible relationship with source depth. Subsets of our results, which were selected by considering the values of dip and rake angles, are shown in Fig. 8a, b, and c. Fig. 8a shows the solutions with at least one dip angle < 45°, while Fig. 8b shows the solutions for both dip angles > 60°. It follows that events in Fig. 8a

UNCORRECTED PROOF

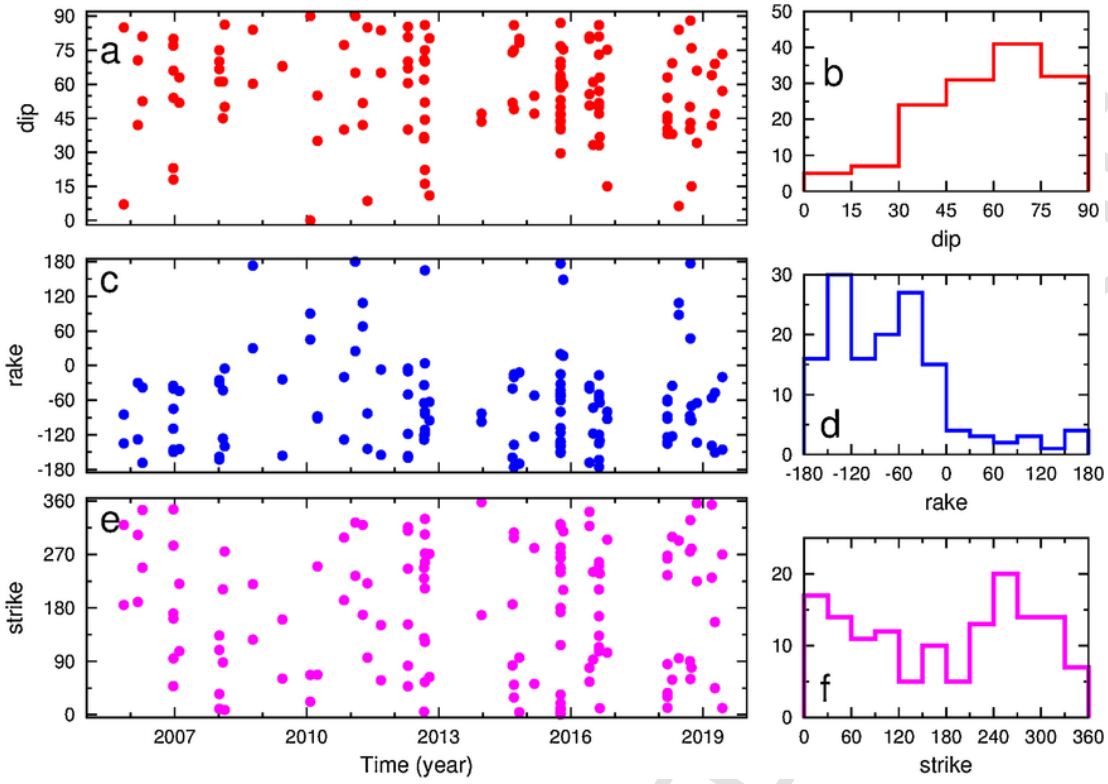

Fig. 6. a) Dip, c) rake, and e) strike angles versus time for both fault and auxiliary planes of the focal mechanisms (Fig. 3). Histogram distributions of b) dip, d) rake, and f) strike angles.

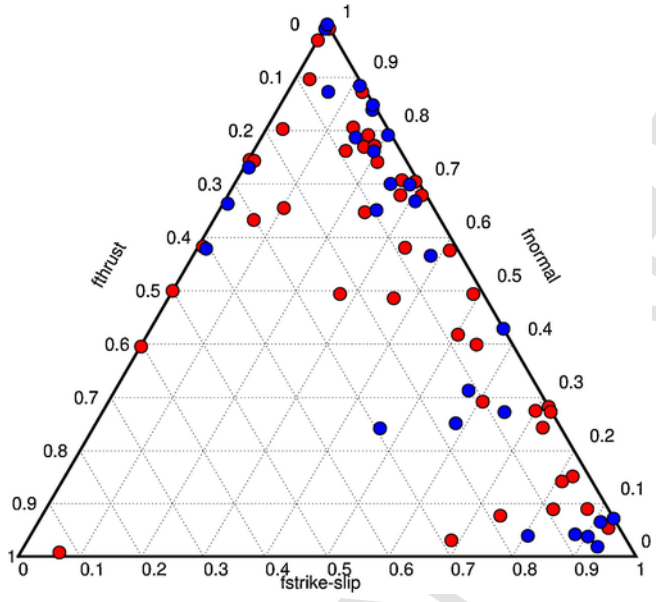

Fig. 7. Ternary plot of the focal mechanism solutions obtained from the method of Frohlich (1999). The axes on the ternary plot identify the relative proportions of strike-slip, normal, and thrust mechanisms. Red and blue symbol correspond to M < 1.5 and $M_D \geq 1.5$, respectively. (For interpretation of the references to colour in this figure legend, the reader is referred to the web version of this article).

cannot therefore appear in Fig. 8b and vice versa. Solutions shown in Fig. 8b represent sources for which both fault and auxiliary planes have a very high angle, therefore their predominant kinematics is strike slip. Fig. 8c shows the solutions that have a dip angle < 60° for both planes, which represent the few earthquakes that had nearly pure normal kinematics. We also searched for a possible relationship between source mechanism and source depth, as shown in Fig. 8 d, e, and f, where the focal mechanisms were selected for three groups of depth ranges: 1) sources at 1–2 km depth (Fig. 8d), 2) sources in the range 2 km < depth < 2.4 km (Figs. 8e), and 3) events with 2.4 km < depth < 3.1 km (Fig. 8f). Two of these ranges are constrained by the shallowest (depth =1 km) and deepest (depth =3.1 km) analysed events. The results did not show any apparent relationship between source kinematics and source depth.

The analysed earthquakes were all very small ($M_D \leq 2.5$), and most of them were located in an area of ~10 km^2 in the central part of the caldera where there are several craters and faults (Orsi et al, 2009; Vitale and Isaia, 2014), thus making it difficult to associate their sources with the main geological structures. On the contrary, it seems that the studied seismicity was mostly associated with many small faults, rather than with a few larger faults.

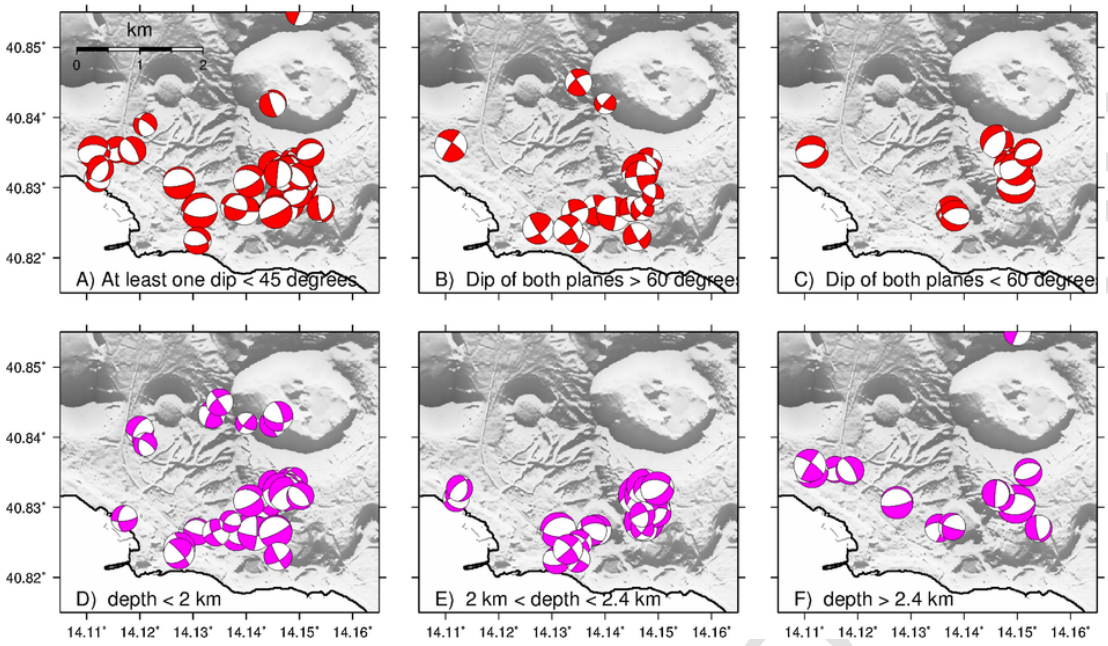

Fig. 8. Selections of focal mechanisms based on the dip angle that considers both planes of the solution (A, B, and C), and selections based on the source depth (D, E, and F).

4. Discussion and conclusions

Our analysis of low magnitude earthquakes that occurred between 2000 and 2019 yielded results that demonstrate a predominance of normal focal mechanisms, a mixture of fault orientations, and many solutions characterised by a high dip-angle. We interpret, therefore, that the main features of recent VT seismicity at the CF caldera include: 1) the location in the area of the highest ground uplift; 2) low magnitudes; 3) shallow source locations; 4) a predominance of normal type focal mechanisms on high angle and nearly vertical faults; and 5) a highly variable nodal plane strike with no clear correlation to the surface features. The predominance of normal kinematics was also observed in the focal mechanisms that were computed for the strongest earthquakes during the 1982–1984 bradyseismic episode (Gaudiosi and Iannaccone, 1984; De Natale et al., 1995), as revised recently through a joint seismological-deformative approach (D'Auria et al., 2015).

Determining the stress field that drives the occurrence of VT earthquake swarms is important for investigating the status of a volcano and provides possible implications regarding the eruption forecast. Thus, based on our focal mechanisms results, we computed the principal stress P and T axes of the associated stress-field using the method proposed by Vavrycuk (2014). This procedure is a modification of the method proposed by Michael (1984), and involves an iterative joint inversion for stress and fault orientations. One of the basic assumptions for calculating the stress field from focal mechanism solutions is that tectonic stress is homogeneous within the investigated area (Gephart and Forsyth, 1984; Roman et al., 2006; Vavrycuk, 2014). This assumption was not fulfilled in our case because the strike distribution did not show any predominant direction. However, since most of the earthquakes had similar kinematics and the strike distribution was not completely uniform, we computed the stress field with the aim of evidencing possible preferential directions that were not clearly apparent in the histograms of Fig. 6. Fig. 9 shows that the σ1 axis falls directly in the middle of the plot, while σ2 and σ3 are both located very near to the border. The P and T axes solutions are widespread without any preferential directions. The σ1 axis that is close to the centre of the circular plot indicates that the main compressive stress is vertically oriented, but with great variability among the analysed events. The σ3 direction is 340°, but the T axes are highly scattered in the polar plot of Fig. 9, with a higher density only in the NNW and SSE directions. The position of σ3 on the border indicates that the average inclination of tensile stress is horizontal.

Hence, the results shown in Fig. 9 so far confirm that the stress field associated with the analysed VT earthquakes was not homogeneous, and cannot be associated with a well-defined direction, as has been reported by many studies, which used the same analysis method for tectonic settings that are characterised by well-defined faults systems (Gephart and Forsyth, 1984; Vavrycuk, 2014; Fojtikova and Vavrycuk, 2018). The scattered epicentre distribution and the shallow location (< 3 km) are compatible with a tensile stress field acting in the shallow part of the

UNCORRECTED PROOF

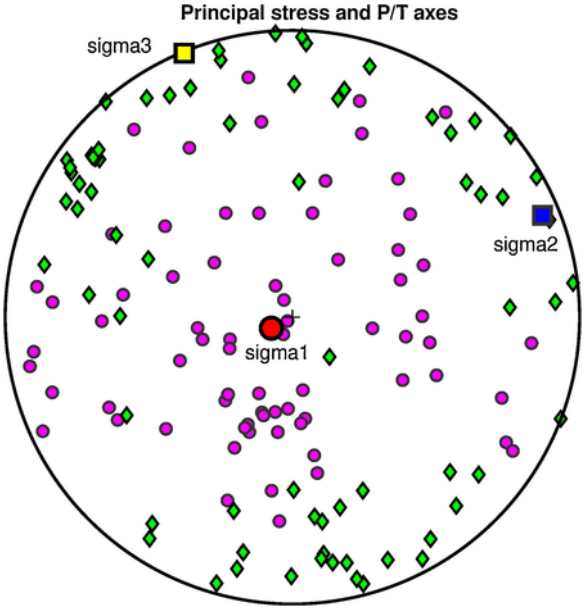

Fig. 9. P and T axes (magenta circles and green diamonds, respectively) corresponding to the computed focal mechanisms shown in Fig. 5 and in Fig. 8. The σ_1, σ_2, and σ_3 stress axes were evaluated by the joint iterative inversion method (Vavrycuk, 2014). (For interpretation of the references to colour in this figure legend, the reader is referred to the web version of this article).

caldera, and are not dependent on the regional stress field. On the other hand, an inflation of the caldera volume caused both ground uplift in the central part and a horizontal elongation of the upper crust. The horizontal elongation of course corresponds to a tensile stress field, which reduces the normal stress acting on high-angle faults, thus favouring the occurrence of normal, dip slip, and strike-slip earthquakes. It is this type of faulting that predominated in our results. On the contrary, no reverse mechanisms were observed in the central area of the CF caldera. This simple interpretation fits very well the observation that VT earthquakes occur mostly during ground uplift, whereas their occurrence is strongly inhibited during subsidence periods. In fact, during subsiding the shallowest part of the crust undergoes a shortening, thus the normal stress on existing high angle and nearly vertical faults increases. This condition reduces the occurrence of earthquakes because the faults are locked. The broad distribution of sources in the central part of the CF caldera is also in good agreement with the hypothesis that the main driving force is the horizontal tensile-stress field that is associated with the ground uplift. On the other hand, the highly variable distribution of strike directions found in our analysis suggests that the role of the regional stress field is negligible in the generation of VT earthquakes in CF. Results of our analysis of focal mechanisms are in good agreement with these hypotheses. In this framework, we conclude that it is reasonable to expect an increasing number of VT earthquakes in the central part of the CF caldera in the near future, at least while the ongoing ground uplift continues.

Uncited references

Di Vito et al. (1999), Gephart and Forsyth (1984), Iannaccone et al. (2018), La Rocca and Galluzzo (2012).

Data availability

Seismic data used in this work are property of Istituto Nazionale di Geofisica e Vulcanologia. Data may be available upon request to the authors of this paper.

Acknowledgement

P. De Martino is gratefully acknowledged for providing the elevation time series of RITE GPS station. Many figures were drawn through the software GMT (Wessel and Smith, 1998). Comments by D. Roman, D. Keir and an anonymous reviewer greatly improved the quality of the paper.

Funding

This research did not receive any specific grant from funding agencies in the public, commercial, or not-for-profit sectors.

References

Acocella, V., 2010. Evaluating fracture patterns within a resurgent caldera: campi Flegrei, Italy. Bull.Volcanol. 72 (2010), 623–638. https://doi.org/10.1007/s00445-010-0347-x.

Antayhua-Vera, Y., Lermo-Samaniego, J., Quintanar-Robles, L., Campos-Enríquez, O., 2015. Seismic activity and stress tensor inversion at Las Tres Vírgenes Volcanic and Geothermal Field (México). J. Vol. Geoth. Res. 305, 19–29.

Aster, R.C., Meyer, R.P., De Natale, G., Zollo, A., Martini, M., Del Pezzo, E., Scarpa, R., Iannaccone, G., 1992. Seismic investigation of the Campi Flegrei Caldera, in "Volcanic seismology". Proc. Volcanol. Ser. III (Springler Verlag, New York)

Cardona, C., Tassara, A., Gil-Cruz, F., Lara, L., Morales, S., Kohler, P., Franco, L., 2018. Crustal seismicity associated to rpid surface uplift at Laguna del Maule Volcanic Complex, Southern Volcanic Zone of the Andes. J. Vol. Geoth. Res. 353, 83–94.

Castellano, M., Buonocunto, C., Capello, M., La Rocca, M., 2002. Seismic surveillance of active volcanoes: the Osservatorio Vesuviano Seismic Network (OVSN – southern Italy). Seism. Res. Lett. 73 (2), 168–175.

Cardellini, C., Chiodini, G., Frondini, F., Avino, R., Bagnato, E., Caliro, S., Lelli, M., Rosiello, A., 2017. Monitoring diffuse volcanic degassing during volcanic unrests: the case of

UNCORRECTED PROOF

Campi Flegrei (Italy). Sci. Rep. 7, 6757. https://doi.org/10.1038/s41598-017-06941-2.
D'Auria, L., Giudicepietro, F., Aquino, I., Borriello, G., Del Gaudio, C., Lo Bascio, D., Martini, M., Ricciardi, G.P., Ricciolino, P., Ricco, C., 2011. Repeated fluid-transfer episodes as a mechanism for the recent dynamics of Campi Flegrei Caldera (1989–2010). J. Geophys. Res. 116, B04313. https://doi.org/10.1029/2010jb007837, 2011.
D'Auria, L., Massa, B., Cristiano, E., Del Gaudio, C., Giudicepietro, F., Ricciardi, G., Ricco, C., 2015. Retrieving the stress field within the Campi Flegrei caldera (Southern Italy) through an integrated Geodetical and Seismological approach. Pure Appl. Geophys. 172, 3247–3263.
Del Gaudio, C., Aquino, I., Ricciardi, G.P., Ricco, C., Scandone, R., 2010. Unrest episodes at Campi Flegrei: a reconstruction of vertical ground movements during 1905–2009. J. Vol. Geoth. Res. 195, 48–56. https://doi.org/10.1016/j.jvolgeores.2010.05.014.
De Martino, P., Tammaro, U., Obrizzo, F., 2014. GPS time series at Campi Flegrei caldera (2000-2013). Ann. Geophys. 57 (2), S0213. https://doi.org/10.4401/ag-6431, 2014.
De Martino, P., Guardato, S., Tammaro, U., Vassallo, M., Iannaccone, G., 2014. A first GPS measurement of vertical seafloor displacement in the Campi Flegrei caldera (Italy). J. Volc. Geoth. Res. 276 (2014), 145–151.
De Natale, G., Zollo, A., Ferraro, A., Virieux, J., 1995. Accurate fault mechanism determination for a 1984 earthquake swarm at Campi Flegrei Caldera during an unrest episode: implications for volcanological research. J. Geophys. Res. 100 (n.B12), 167–24,185, 10 december 1995.
Di Vito, M.A., Isaia, R., Orsi, G., Southon, J., de Vita, S., D'Antonio, M., Pappalardo, L., Piochi, M., 1999. Volcanism and deformation since 12000 years at the Campi Flegrei caldera (Italy). J Volcanol Geotherm Res 91, 221–246.
Di Vito M.A., Acocella V, Aiello G., Barra D., Battaglia M., Carandente A., Del Gaudio C., De Vita S., Ricciardi G.P., Ricco C., Scandone R., Terrasi F., Magma transfer at Campi Flegrei caldera (Italy) before the 1538 AD eruption. Sci. Rep. 6, 32245; doi: 10.1038/srep32245 (2016).Frohlich, C., 1992. Triangle diagrams: ternary graphs to display similarity and diversity of earthquake focal mechanisms. Phys. Earth Planet. Inter. 75, 193–198.
Fojtikova, L., Vavrycuk, V., 2018. Tectonic stress regime in the 2003–2004 and 2012–2015 earthquake swarms in the Ubaye Valley, French Alps. Pure App. Geophys. 175 (2018), 1997–2008.
Gaudiosi, G., Iannaccone, G., 1984. A preliminary study of stress pattern at Phlegraean Fields as inferred from focal mechanisms. Bull. Volcanol.47–2.
Gephart, J.W., Forsyth, D.W., 1984. An improved method for determining the regional stress tensor using earthquake focal mechanism data: application to the San Fernando earthquake sequence. J. Geophys. Res. 89 (B11), 9305–9320.
Hopp, C.J., Waite, G.P., 2016. Characterization of seismicity at Volcán Barú, Panama: may 2013 through April 2014. J. Vol. Geoth. Res. 328, 187–197.
Iannaccone, G., Guardato, S., Donnarumma, G.P., De Martino, P., Dolce, M., Macedonio, G., Chierici, F., Beranzoli, L., 2018. Measurement of seafloor deformation in the marine sector of the Campi Flegrei caldera (Italy). J. Geophys. Res. Solid Earth 123, 66–83.
Judson, J., Thelen, W.A., Greenfield, T., White, R.S., 2018. Focused seismicity triggered by flank instability on Kilauea's Southwest Rift Zone. J. Vol. Geoth. Res. 353, 95–101.
Konstantinou, K.I., Lin, C.H., Liang, W.T., Chan, Y.C., 2009. Seismogenic stress field beneath the Tatun Volcano Group, northern Taiwan. J. Vol. Geoth. Res. 187, 261–271.
La Rocca, M., Galluzzo, D., 2012. A seismic array in the town of Pozzuoli in Campi Flegrei (Italy) Seism. Res. Lett. 83 (n. 1), 86–96. https://doi.org/10.1785/gssrl.83.1.86.
La Rocca, M., Galluzzo, D., 2015. Seismic monitoring of Campi Flegrei and Vesuvius by stand-alone instruments. Ann. Geophys. 58 (5), S0544. https://doi.org/10.4401/ag-6748, 2015.
Li, K.L., Abril, C., Gudmundsson, O., Gudmundsson, G.B., 2019. Seismicity of the Hengill area, SW Iceland: details revealed by catalog relocation and collapsing. J. Vol. Geoth. Res. 376 (2019), 15–26.
Michael, A.J., 1984. Determination of stress from slip data: faults and folds. J. Geophys. Res. 89 (B13), 11517–11526.
Orsi, G., Civetta, L., Del Gaudio, C., De Vita, S., Di Vito, M.A., Isaia, R., Petrazzuoli, S.M., Ricciardi, G.P., Ricco, C., 1999. Short-term ground deformations and seismicity in the resurgent Campi Flegrei caldera (Italy) an example of active block-resurgence in a densely populated area. J. Volc. Geoth. Res. 91, 415–451.
Orsi, G., Di Vito, M.A., Isaia, R., 2004. Volcanic hazard assessment at the restless Campi Flegrei caldera. Bull. Volcanol. 66, 514–530. https://doi.org/10.1007/s00445-003-0336-4.
Orsi, G., Di Vito, M.A., Selva, J., Marzocchi, W., 2009. Long-term forecast of eruption style and size at Campi Flegrei caldera (Italy). Earth Plan. Sci. Lett. 287 (2009), 265–276.
Reyners, M., 2010. Stress and strain from earthquakes at the southern termination of the Taupo Volcanic Zone, New Zealand. J. Vol. Geoth. Res. 190, 82–88.
Roman, D.C, Neuberg, J., Luckett, R.R., 2006. Assessing the likelihood of volcanic eruption through analysis of volcanotectonic earthquake fault–plane solutions. Earth Planet. Sci. Lett. 248 (2006), 244–252.
Saccorotti, G., Bianco, F., Castellano, M., Del Pezzo, E., 2001. The July-August 2000 seismic swarms at Campi Flegrei volcanic complex, Italy. Geophys. Res. Lett. 28 (13), 2525–2528, july 1, 2001.
Saccorotti, G., Petrosino, S., Bianco, F., Castellano, M., Galluzzo, D., La Rocca, M., Del Pezzo, E., Zaccarelli, L., Cusano, P., 2007. Seismicity associated with the 2004-2006 renewed ground uplift at Campi Flegrei caldera, Italy. Phys. Earth Planet. Inter. https://doi.org/10.1016/j.pepi.2007.07.006.
Snoke, J.A., Munsey, J.W., Teague, A.C., Bollinger, G.A., 1984. A program for focal mechanism determination by combined use of polarity and SV -P amplitude ratio data. Earthquake Notes 55 (#3), 15.
Snoke, J.A., 1989. In: James, D.E. (Ed.), Earthquake Mechanisms, Encyclopedia of Geophysics. Van Nostrand Reinhold Company, New York, pp. 239–245.
Vavrycuk, V., 2014. Iterative joint inversion for stress and fault orientations from focal mechanisms. Geophys. J. Int. 199, 69–77.

UNCORRECTED PROOF

Vitale, S., Isaia, R., 2014. Fractures and faults in volcanic rocks (Campi Flegrei, southern Italy): insight into volcano-tectonic processes. Int J Earth Sci (Geol Rundsch) 103 (2014), 801–819. https://doi.org/10.1007/s00531-013-0979-0.

Wessel, P., Smith, W.H.F., 1998. New, improved version of the Generic Mapping Tools released. EOS Trans AGU 79, 579.

UNCORRECTED PROOF